# *Secondary Flow Behavior and Particle Transport in Bifurcations*

*Fong Yew Leong*[a], *Kenneth A. Smith*[a,b], *Chi-Hwa Wang*[a,c]
[a] *MEBCS Program, Singapore-MIT Alliance*
[b] *Department of Chemical Engineering, Massachusetts Institute of Technology,*
[c] *Department of Chemical and Biomolecular Engineering, National University of Singapore*

Prepared for presentation at the 2005 AIChE Annual Meeting

Cincinnati, Ohio, October 30 - November 4, 2005.

September, 2005

## Introduction

The secondary flow behavior in bifurcation models is of great importance to health risk assessments and pulmonary drug delivery. Sub-micron aerosols are commonly inhaled from the ambient environment, workplace or therapeutic inhalers. Studies have shown that, due to their deep lung penetration capability, many types of sub-micron toxic aerosols are potentially more hazardous than their micron-sized counterparts [1, 2]. Or, in the case of therapeutic aerosols, smaller drug particles can also be more efficient tools for drug delivery [3].

The dominant deposition mechanism of ultrafine particles is Brownian diffusion, as opposed to inertial impaction and sedimentation for larger particles. Hence, for ultrafine particles, an adequate description of the deposition can be obtained from solutions to the fluid momentum equations and the convective diffusion equation. Preliminary numerical (FEMLAB) studies on a 2-D single bifurcation have been conducted by invoking order of magnitude arguments at high Schmidt numbers [4].

Steady flow in single bifurcation models yields the familiar counter-rotating vortices in the inspiratory phase, but more complicated flow patterns develop in double or triple bifurcation models [5, 6]. Previous numerical efforts have shown that the secondary flows in the double bifurcation can yield another set of counter-rotating vortices in the opposite sense to the Dean’s vortices, but how they are actually formed remains unclear. This part of the study focuses on the analysis of the vortex generation phenomenon and the relationship with transport of ultrafine particles.

## 3-D Numerical Solution

3-D laminar steady flow of incompressible viscous fluid in a double bifurcation model is to be considered here. A physiological value of 0.9 is prescribed for the ratio of daughter tube diameters to the preceding parent tube diameters, and the average length to diameter ratio is set at 3. It is computationally efficient to use one of the symmetrical half of the double bifurcation model and therefore, the length-scale of choice in this problem is the radius of the parent tube, written as L. The geometric description of the problem is presented in Fig. 1, where fully developed flow at the inlet is assumed.

There is currently no known analytic solution to flow in bifurcation problems. The generic equations to be solved are the complete set of Navier-Stokes equation and the continuity equation.

$$\rho(\bar{v} \cdot \nabla \bar{v}) = \rho g - \nabla P + \mu \nabla^2 \bar{v} \tag{1}$$

$$\nabla \cdot \bar{v} = 0 \tag{2}$$

where ρ is fluid density, $\bar{v}$ is the fluid velocity, μ is kinematic viscosity and P is pressure.

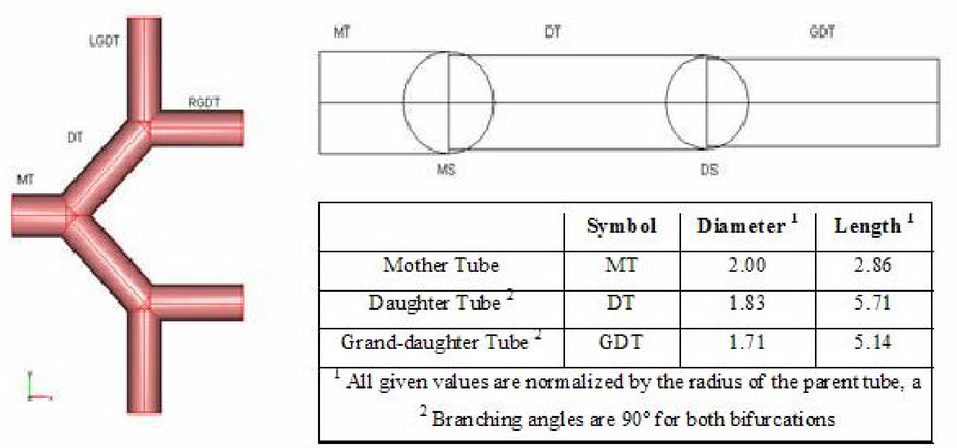

| | Symbol | Diameter [1] | Length [1] |
|---|---|---|---|
| Mother Tube | MT | 2.00 | 2.86 |
| Daughter Tube [2] | DT | 1.83 | 5.71 |
| Grand-daughter Tube [2] | GDT | 1.71 | 5.14 |

[1] All given values are normalized by the radius of the parent tube, a

[2] Branching angles are 90° for both bifurcations

**Fig 1. Geometric description of double bifurcation model (3-D)**

The solution to the fluid momentum equations can be obtained through various numerical methods and commercial CFD packages. For this case, FEMLAB has been used. The number of finite elements used is approximately 114,000 and the Reynolds number at the inlet of the parent tube is 420. The fluid flow can be visualized using a streamline plot as shown in Fig. 2. Velocities as shown have been normalized against the maximal centerline velocity. The peak centerline flow at the mother tube first encounters the emerging boundary layer at the carinal ridge and the axial velocity is reduced due to the efflux of vorticity from the wall. The slower moving fluid near the walls of the carinal ridge migrates outwards along the circumferential boundary of the daughter tube, to be replaced by the faster moving core fluid. This exchange of momentum due to the secondary pressure gradient sets up a pair of counter-rotating vortices, which is not unlike the solution from the classical curved tube problem.

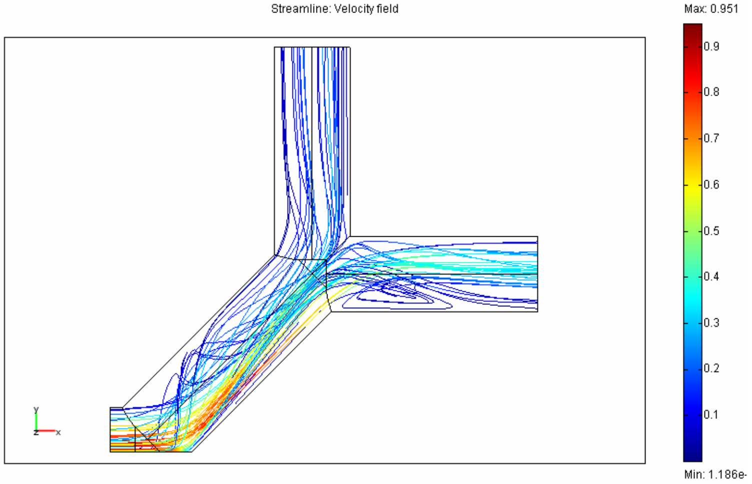

**Fig 2. Plot of velocity streamlines (Re 420, Top-down 3-D) – Colormap refers to normalized velocity**

The results at the characteristic Reynolds number also predicted flow separation at two major locations in the model, namely at the outer walls of the daughter tubes and the inner grand-daughter tubes, followed by reattachment downstream. The presence of flow separation in the bifurcation context generally depends on a number of parameters, including branch angle, Reynolds number, the area and curvature ratios, but this result agrees qualitatively with the literature (e.g. [7]). Close examination of the numerical solution of the double bifurcation configuration reveals the presence of a new pair of counter-rotating vortices at the grand-daughter tubes. It is interesting to note that this set of vortices is directly opposite in sense to what is expected from Dean's result. This phenomenon can also be found in some of the more detailed CFD studies of this problem [6], but unfortunately there has been very little progress in our understanding, despite its obvious physiological significance.

The major source of difficulty is the lack of theoretical understanding of the fluid dynamics in the 3-D bifurcation geometry with upstream influence. Every effort must be made to condense the problem to a manageable level. It is desirable to understand how the anti-sense vortices are formed at the fundamental level.

## Theoretical Development

Consider the three-dimensional single bifurcation geometry as shown in Fig. 3. Since the object of interest is at the second bifurcation, let the daughter tube (DT) be the parent tube and the grand-daughter tubes (LGDT and RGDT) in this case. Let AOB be the pivoting centreline of the bifurcation, where A and B are the intersecting points between the pivoting axis and the wall boundaries, and C be the centre of the carinal ridge. The bifurcation angle is set as 2α.

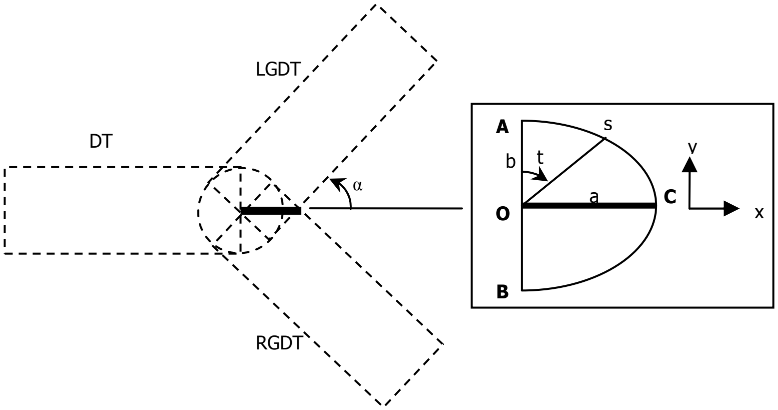

**Fig 3. Geometric description of model**

For simplicity, we consider the 2-D semi-elliptic plane denoted by AOBC, where ACB is the carinal ridge wall boundary. The upstream condition at AOB is established numerically, through the solution of the entire double bifurcation problem. It should be noted that continuity is not satisfied on the 2-D domain since there is no outflow boundary. We are also assuming that there is no significant efflux of momentum in the direction normal to the plane AOBC and this has been numerically verified to valid within the context of the problem. The enforced no-penetration condition of the wall arc ACB also means that each streamline on the plane AOBC is a stagnation streamline and the subsequent analysis is essentially static.

It is convenient to describe this geometrical form using a set of parametric equations. Now the arc-length can be rewritten in the form of an incomplete elliptic integral,

$$s = \int_0^t \left( \sqrt{1-(\sin\alpha \sin t)^2} \right) dt \tag{3}$$

where t is the parametric angle $0 \le t \le \pi$ , and $\alpha(t) = \arctan(-\cos\theta \tan t)$ with θ being the bifurcation angle and it represents the influence of the third dimensional length on the 2-D problem. In the model, we make the assumption that the entrance fluid is irrotational and the fluid streamlines are parallel to OC. The model assumes that each fluid element encounters no drag until it encounters the wall where velocity reduces to zero and exits the plane to the left or right daughter tube. We therefore apply the classical Bernoulli's equation to the inlet velocity profile as a function of angle t, neglecting gravitational effects.

$$P(t) \sim \left(\frac{\rho U(t)^2}{2}\right)\left[\underset{normal}{\sin^2 \alpha(t)} + \underset{\tan gential}{\cos^2 \alpha(t)}\right] + P_\infty \tag{4}$$

Neglecting viscous shear and other boundary layer effects, the pressure at the wall is estimated to be the kinetic energy as converted to pressure. The pressure profile so obtained is normalized against ($\rho U^2/2$) and plotted alongside the results obtained directly from FEMLAB, as a function of t in radians, as shown in Fig. 4a and Fig. 4b, for the first and second bifurcations respectively. t = 0 corresponds to point A, t = 1.57 corresponds to point C, and t = 3.14 corresponds to point B.

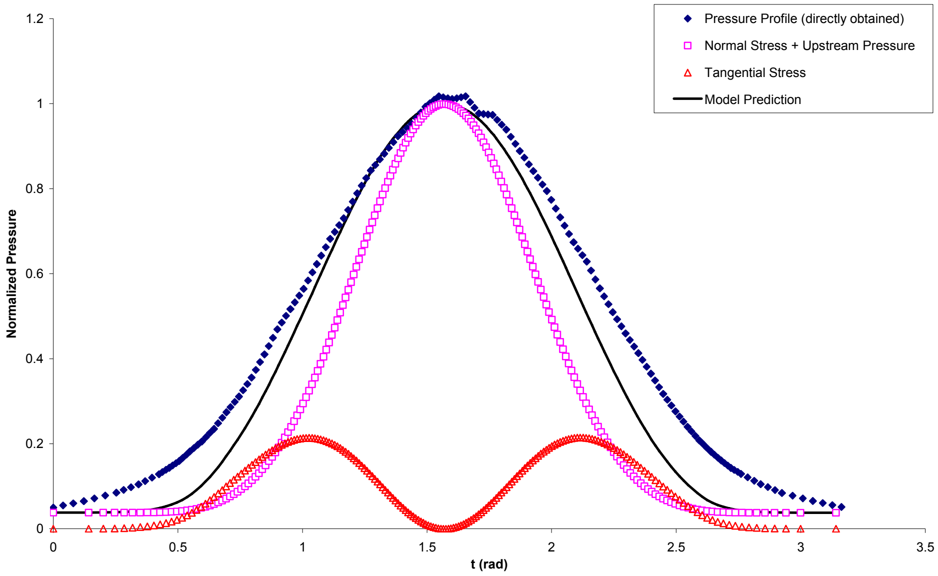

**Fig 4a. Pressure Profile at Arc ACB for 1st Bifurcation (Re 420)**

There is close agreement between the Bernoulli's predictions and the numerical result for the case of the *first* bifurcation, as observed in Fig. 4a. The parabolic fully developed velocity profile at the inlet creates very high normal stresses at the centre of the carinal ridge t = π/2, which decreases monotonically to the ends A (t = 0) and B (t = π). These results suggest that this is a reasonable, if highly simplified, approach to the analysis of the complicated 3-D problem.

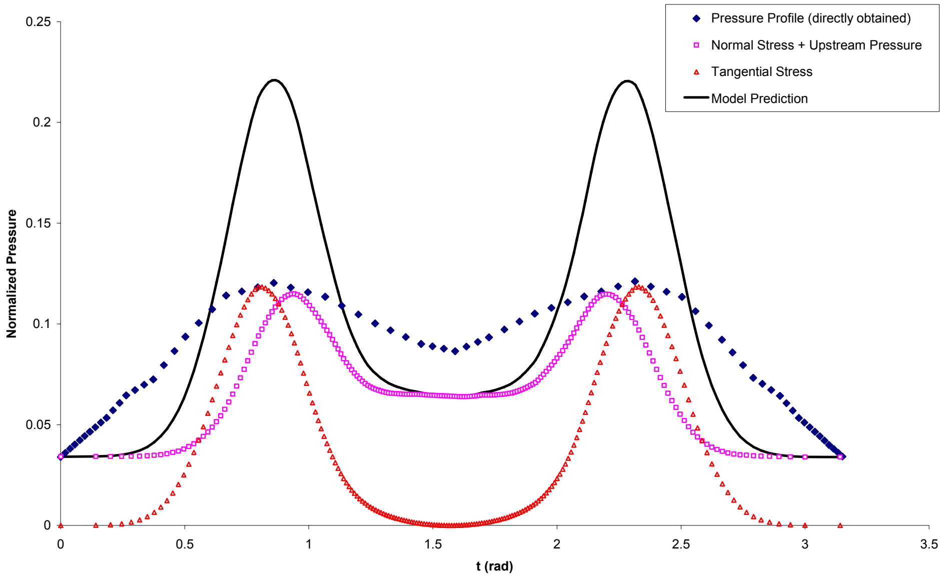

**Fig 4b. Pressure Profile at Arc ACB for 2nd Bifurcation (Re 420)**

On the other hand, there is significant deviation between the Bernoulli result and the numerical result for the *second* bifurcation (Fig. 4b). This is an interesting observation, and highlights the fundamental differences between the two bifurcations even though they are both geometrically self-similar. The crucial difference here is that the upstream velocity condition for the second bifurcation is not fully developed, unlike the case for the first bifurcation. The entrance flow normal to ACB is the 'M-shaped' velocity profile, as was also observed experimentally by several workers on this subject [8].

The mismatch of the profiles as shown in Fig 4b suggests that is transfer of momentum occurring within plane AOBC, which might lead to the emergence of the observed vortices. Consequently, the computed pressure profiles as presented in Fig 4b is integrated from Point A (t =0) to Point C (t = π/2), while taking full advantage of the inherent symmetry afforded by the semi-elliptic plane. This re-plot yields a profile of cumulative force against arc-length as shown in Fig. 5.

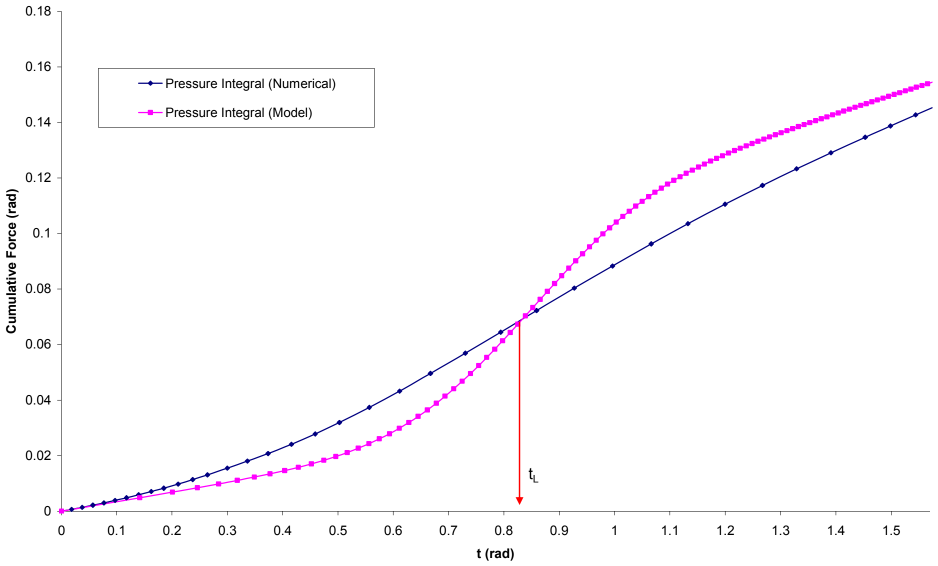

**Fig 5. Cumulative Force Profile at Arc ACB for 2nd Bifurcation (Re 420)**

Fig 5 complements the earlier Fig 4b in two ways. One is the error assessment for the conservation of linear momentum, which is the justifiably small deviation of the curves at Point C (t = π/2). The other is the intersection between the two curves ($t_L$ = 0.83 in this case), where the cumulative force balance is satisfied. This limiting parametric angle $t_L$ is important, for it is the imaginary location where there is no preferred torque in either direction of the arc-angle. The consequence of this statically stable stagnation streamline is that the fluid to the left of this limiting angle tends to rotate anti-clockwise and the fluid to the right tends to rotate clockwise.

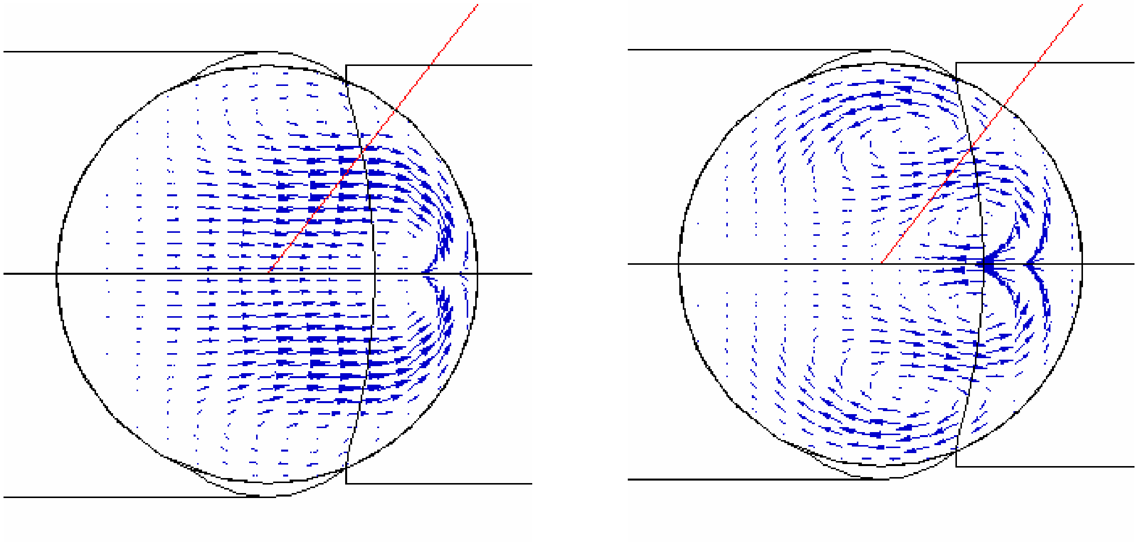

**Fig 6. Normalized Secondary Flow Velocity Profiles in LGDT (Left: Carinal Ridge Plane AOBC; Right: 0.5L downstream) – Red line denotes the limiting angle $t_L$ as obtained in Fig. 5**

Fig 6 shows the normalized secondary flow velocity profiles in the grand-daughter tube (GDT) for the cross section of the carinal ridge at AOBC (Left) and one-half characteristic length downstream. The counter-rotating vortices are observed to have opposite sense to the Dean's vortices. In addition, the red line shown in Fig. 6 is the limiting parametric arc angle as determined from Fig 5. It is clearly a good estimate for the dividing plane between the vortices, as expected theoretically.

For the case of transport of ultrafine particles in bifurcations, one important implication of this work is that the region of maximum mass deposition is not at the center of the carinal ridge (Point C) for the second bifurcation. In fact, for convective dominated transport, we expect a double maximum for mass deposition along arc ACB (for an arc-angle from 0 to π): one close to $t_L$ and the other close to π- $t_L$ on the other quadrant. For clarification, the steady convective-diffusive equation has been solved numerically based on the solution for the steady fluid momentum equations for the fluid phase.

$$\bar{v}\nabla C = D\nabla^2 C \tag{3}$$

where C is the normalized concentration and D is the Brownian diffusion coefficient, taken to be 6.8e-6 (~1nm particles). The wall boundary condition is null concentration [4]. Based on unit parent tube inlet concentration, the radial Sherwood number of the LGDT is obtained as a function of the parametric angle t and plotted as shown in Fig 7 for various axial downstream distances.

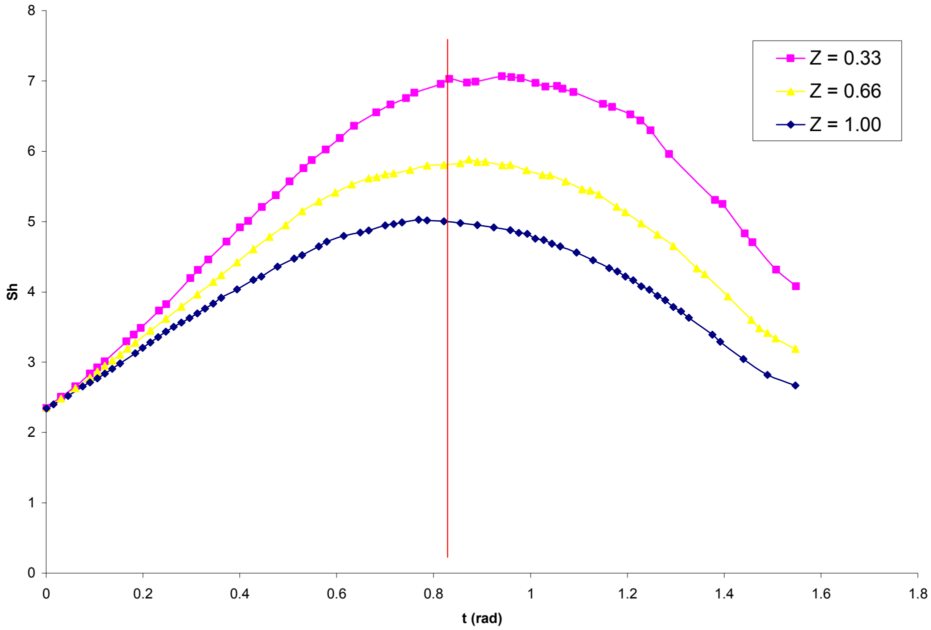

**Fig 7. Plot of Radial Sherwood Number as function of t in LGDT (Legend denotes dimensionless downstream axial distance Z) – Red line denotes the limiting angle $t_L$ as obtained in Fig. 5**

Fig 7 shows that the maximum radial Sherwood number in fact translates along the parametric angle t with increasing downstream axial distance. The next step is to determine the dependence of wall mass flux on the intensity and sense of the vortices in the grand-daughter tubes. This is again subjected to dimensional analysis [4].

## Reference

[1] M.W. Frampton, Systemic and cardiovascular effects of airway injury and inflammation: ultrafine particle exposure in humans, Environ. Health Perspectives 109, 529-532, 2001.

[2] K. Donaldson, X.Y. Li, W. Macnee. Ultrafine (nanometer) particle-mediated lung injury. J. Aerosol Sci. 29, 553-560, 1998.

[3] D.A. Edwards. Delivery of biological agents by aerosols. AIChE J. 48(1), 2-6, 2002.

[4] Leong F.Y., Smith K.A., Wang C.H. Transport of Submicron Aerosols in Bifurcations. Singapore-MIT Alliance Annual Symposium, MEBCS, 2005

[5] Ertbruggen C., Hirsch C., Paiva M., Anatomically based three-dimensional model of airways to simulate flow and particle transport using computational fluid dynamics. J. Appl. Physiol. 98, 970-980, 2005

[6] Zhang Z., and Kleinstreuer C. Transient airflow structures and particle transport in a sequentially branching lunch airway model. Phys. Fluids 14(2), 862-880, 2002

[7] Pedley, T.J., Schroter R.C., Sudlow, M.F. Gas flow and mixing in the airways. In Bioengineering Aspects of the Lung (ed J.B. West), 163-265, 1977

[8] Pedley T.J. The Fluid Mechanics of Large Blood Vessels. Cambridge University Press. 1980.